Chinese Journal of Catalysis 79 (2025) 78–90

available at www.sciencedirect.com

ScienceDirect

journal homepage: www.sciencedirect.com/journal/chinese-journal-of-catalysis

Article

Optimized kinetic pathways of active hydrogen generation at Cu_2O/Cu heterojunction interfaces to enhance nitrate electroreduction to ammonia

Xi Chen [a,1], Wei Jin [a,1], Xinyu Zhong [c], Hongqiao Lin [b], Junjie Ding [d], Xinyu Liu [a], Hui Wang [a], Fasheng Chen [a], Yan Xiong [b,*], Changchun Ding [a,*], Zhong Jin [b,*], Minghang Jiang [a,b,*]

[a] *Department of Chemistry, School of Science, Xihua University, Chengdu 610039, Sichuan, China*

[b] *State Key Laboratory of Coordination Chemistry, MOE Key Laboratory of Mesoscopic Chemistry, MOE Key Laboratory of High Performance Polymer Materials and Technology, Jiangsu Key Laboratory of Clean Energy Catalysis and Intelligent Green Chemical Engineering, Suzhou Key Laboratory of Green Intelligent Manufacturing of New Energy Materials and Devices, Tianchang New Materials and Energy Technologies Research Center, Institute of Green Chemistry and Engineering, School of Chemistry and Chemical Engineering, Nanjing University, Nanjing 210023, Jiangsu, China*

[c] *Shanghai Institute of Applied Physics, Chinese Academy of Sciences, Shanghai 201800, China*

[d] *College of Physics and Center of Quantum Materials and Devices, Chongqing University, Chongqing 401331, China*

ARTICLE INFO

Article history:
Received 4 July 2025
Accepted 23 August 2025
Available online 5 December 2025

Keywords:
Modulation of the active hydrogen concentration
Adjusting the Co doping form
Electrocatalytic nitrate reduction reaction
Electrocatalytic ammonia synthesis

ABSTRACT

In this paper we report the preparation of nano-dendritic Cu_2O/Cu heterojunctions doped with varying concentrations of cobalt through a convenient, energy-consumption-free, and environmentally friendly chemical replacement method. The analysis results reveal that the incorporation of cobalt in its atomic form enhances the adsorption of nitrate species onto the catalyst surface, whereas doping with metallic cobalt promotes the production of active hydrogen (*H). By adjusting the doping concentration of cobalt, we effectively control its doping form (atomic and metallic states) on the surface of dendritic copper, thereby enabling controllable modulation of the active hydrogen concentration on the catalyst surface. By ensuring sufficient consumption of *H during the NITRR process while avoiding excessively high concentrations that could trigger detrimental hydrogen evolution reaction side reactions, this approach remarkably enhances the selectivity of ammonia synthesis in NITRR. This study offers an effective approach to regulate the *H concentration on the surface of the catalyst through adjusting the metal doping form, thereby improving the performance of ammonia synthesis from NITRR.

1. Introduction

Ammonia (NH_3) stands as a pivotal chemical in contemporary society, playing a crucial role in the production of fertiliz-

* Corresponding author. E-mail: xiongyan@nju.edu.cn (Y. Xiong), ccding626@163.com (C. Ding), zhongjin@nju.edu.cn (Z. Jin), minghang@mail.xhu.edu.cn (M. Jiang).

[1] Contributed equally to this work.

This work was supported by the National Natural Science Foundation of China (22561160129, 22479074, 22475096), the Natural Science Foundation of Sichuan Prov-ince (2023NSFSC1074, 2023NSFSC0909), the Talent Introduction Plan of Xihua University (Z222051), the General Project of the Joint Fund of Equipment Pre-research and the Ministry of Education (8091B02052407), the Fundamental Reaearch Program Key Project of Jiangsu Province (BK20253008), the Natural Science Foundation of Jiangsu Province (BK20240400, BK20241236), the Science and Technology Major Project of Jiangsu Province (BG2024013), the Scientific and Technological Achievements Transformation Special Fund of Jiangsu Province (BA2023037), the Academic Degree and Postgraduate Education Reform Project of Jiangsu Province (JGKT24_C001), the Key Core Technology Open Competition Project of Suzhou City (SYG2024122), the Open research fund of Suzhou Laboratory (SZLAB-1308-2024-TS005), and the Chenzhou National Sustainable Development Agenda Innovation Demonstration Zone Provincial Special Project (2023sfq11).
https://doi.org/10.1016/S1872-2067(25)64848-0

ers, pharmaceuticals, and numerous other industrial applications [1–4]. Currently, the production of NH_3 predominantly depends on the Haber-Bosch (H-B) process, which operates under severe conditions of high temperature and pressure, and contributes to over 1% of global greenhouse gas emissions [5,6]. Hence, there is a pressing necessity to develop an environmentally benign and sustainable technology for NH_3 synthesis. To achieve this goal, electrochemical NH_3 synthesis employing nitrogen-containing species (like N_2 and NO_3^-) and H_2O as reactants, offers a promising method for sustainable NH_3 production. While N_2 dissociation demands 941 kJ·mol^{-1} to break its strong N≡N bond, nitrate in the NITRR undergo deoxygenation with a markedly lower energy barrier of only 204 kJ·mol^{-1} [5,7]. Furthermore, NO_3^- solubility is roughly 40000 times greater than N_2 [8,9].

Another significant merit of nitrate utilization lies in its widespread natural abundance. Specifically, global fossil fuel combustion, extensive application of nitrogen-based fertilizers, industrial wastewater discharge with nitrate concentrations up to 2×10^{-3} mol·L^{-1} and extensive reserves of niter ores (predominantly located in Chile and China's Turpan Basin) collectively bring about an extremely rich nitrate supply in the natural environment [10–12]. Moreover, it is important to note that an excessive accumulation of nitrate in drinking water can potentially pose health risks to humans [13–15]. Therefore, the electrochemical NITRR emerges as a promising method for recycling nitrogen, mitigating environmental contamination, and concurrently yielding value-added ammonia.

The electrochemical NITRR to NH_3 involves a complex process requiring nine protons and eight electrons, as depicted by the reaction equation $NO_3^- + 9H^+ + 8e^- \rightarrow NH_3 + 3H_2O$ (E = −1.2 V *vs.* standard hydrogen electrode), which has slow kinetics [4,16–18]. Meanwhile, the presence of the competitive HER alongside numerous byproducts complicates the reaction pathways, resulting in undesirable consumption of electrical energy and subsequently diminishing the selectivity and efficiency of the NITRR [19]. Therefore, it is highly desirable to design catalysts that exhibit a highly-selectivity for electrocatalytic NITRR for ammonia synthesis.

Currently, Cu-based catalysts remain prominent options for achieving high selectivity in the electrochemical reduction nitrate [4,20–22]. This is attributed to excellent electrical conductivity of Cu and its 3d orbital being fully occupied. The distinctive $3d^{10}$ electron configuration of Cu allows its exceptional catalytic activity for NO_3^- reduction [5,12]. Thus far, a diverse array of strategies has been formulated for the design of Cu–based catalysts aimed at augmenting electrocatalytic NITRR efficacy [23,24]. These strategies encompass a multitude of facets, including the meticulous control of catalyst size (such as single atoms [24,25], nanoclusters [18,20,27], and nanoparticles [21,28,29], the modulation of morphology and crystal plane orientations [30–32], the engineering of surface defects [33,34], the incorporation of dual active sites [35–38], and the doping of Cu-based materials with heteroatoms [39], among several others. However, the commercial implementation of previously developed Cu-based electrocatalysts is impeded by their environmentally unsustainable nature, complex synthesis processes, and limited small-batch production capabilities.

Consequently, there is currently a paucity of research concentrating on the rapid, green and scalable synthesis of Cu-based nanostructured electrocatalysts that simultaneously enhance both the activity and durability of nitrate reduction to ammonia. In addition, copper demonstrates suboptimal proton activation capacity, suppressing surface *H generation and consequently retarding the *H supply kinetics, which ultimately restricts NO_3^- electroreduction to NH_3 [40–42]. Specifically, electrochemical NITRR process encompasses the deoxygenation of nitrate (NO_3^-) to form intermediate species including nitrite (*NO_2), nitric oxide (*NO), and nitrogen (*N), followed by the hydrogenation of *N to produce ammonia intermediates like *NH, *NH_2, and ultimately NH_3 [22,43,44]. Active hydrogen is pivotal for NH_3 synthesis in the NITRR process, with its concentration exerting a profound influence on the Faradaic efficiency for NH_3 (FE_{NH3}) [17,45,46].

Insufficient concentrations hinder the smooth progression of NH_3 synthesis within the NITRR process, whereas excessively high concentrations can induce vigorous HER, resulting in decreased NH_3 production. Hence, the regulation of active hydrogen concentration on copper-based catalyst surfaces to attain a dynamic equilibrium between its production and consumption within the nitrate reduction to ammonia process is pivotal for optimizing both the selectivity and kinetics of ammonia synthesis. However, the controllable modulation of active hydrogen concentration on the surface of copper-based catalysts remains a challenging research endeavor, with limited studies reported to date. Additionally, previous studies have demonstrated that doping cobalt sites into the catalyst structure is beneficial for facilitating water molecule activation, thereby ensuring a consistent and reliable generation of *H intermediates during NO_3^- reduction process NO_3^- [47–49]. However, the underlying mechanisms by which different forms of cobalt doping influence the electrochemical NITRR process, as well as how to fine-tune and optimize the kinetic pathways for generating active hydrogen on the catalyst surface by adjusting the cobalt doping concentration, remain areas that warrant further exploration.

Herein, we report the preparation of nano-dendritic heterojunctions doped with various concentrations of cobalt (Co_x-Cu_2O/Cu, x = 0.05, 0.10, or 0.34) through a convenient, energy-consumption–free and environmentally friendly chemical replacement method. By adjusting the doping concentrations of cobalt, we have successfully induced a controlled transition of cobalt doping at the Cu_2O/Cu heterojunction interfaces, transitioning from an atomic state to metallic cobalt. The combination of experimental data and theoretical calculations reveals that atomic cobalt doping enhances the adsorption of nitrate reaction species onto the catalyst surface, whereas metallic cobalt doping facilitates the production of active hydrogen. By fine-tuning the doping concentration of cobalt within dendritic copper structures, we have achieved a modulation in the ratio of cobalt doping forms (atomic and metallic), thereby effectively regulating the concentration of active hydrogen on

the surface of electrocatalyst. This regulation enables the maintenance of a dynamic equilibrium between the production and consumption of *H during NITRR process. This obtained $Co_{0.10}$-Cu_2O/Cu catalyst exhibited an impressive NH_3 yield of 290.0 μmol·h^{-1}·mg$^{-1}_{cat.}$ and a FE_{NH3} of 86.2% at −0.7 V *vs.* reversible hydrogen electrode (RHE), greatly surpassing the performance of pristine Cu_2O/Cu, which yielded 51.0 μmol·h^{-1}·mg$^{-1}_{cat.}$ and an FE_{NH3} of 32.5%, respectively. Notably, the $Co_{0.10}$-Cu_2O/Cu catalyst demonstrated notable stability, maintaining nearly unaltered catalytic activity following successive cycle tests and extended evaluations. This work offers significant guidance for the subsequent rapid, convenient, and large-scale preparation of dendritic copper catalysts. Additionally, it presents a novel approach for the controllable modulation of active hydrogen concentrations on copper-based catalyst surfaces through adjusting the doping concentration of heteroatoms, thereby mitigating HER side reactions and enhancing NITRR selectivity.

2. Experimental

2.1. Synthesis of dendritic Cu_2O/Cu and cobalt-doped dendritic Cu_2O/Cu (Co_x-Cu_2O/Cu, x = 0.05, 0.10, or 0.34) samples

Dendritic Cu_2O/Cu sample was synthesized via a rapid and convenient chemical replacement method. Specifically, a piece of Zn foil (3×3 cm^2) was sequentially cleaned by acetone, deionized water and ethanol. Subsequently, the cleaned Zn foil was immersed in a 500 mmol·L^{-1} $CuCl_2$ solution for 4 min, followed by the removal of excess Zn foil. During this process, the Zn foil undergoes a displacement reaction with $CuCl_2$ to form a powdered dendritic Cu_2O/Cu sample. The formation of Cu_2O on the surface of dendritic Cu_2O/Cu sample may originate from the oxygen present in both the solution and the air. Subsequently, the resulting powder was washed with deionized water and ethanol, and subsequently vacuum-dried at 50 °C. Similarly, dendritic Cu_2O/Cu samples with varying cobalt doping concentrations (Co_x-Cu_2O/Cu, *x* = 0.05, 0.10, or 0.34) were synthesized using the same preparation method as for dendritic Cu_2O/Cu, except that the 500 mmol·L^{-1} $CuCl_2$ solution was replaced with 300 mmol·L^{-1} $CuCl_2$ + 200 mmol·L^{-1} $CoCl_2$, 200 mmol·L^{-1} $CuCl_2$ + 300 mmol·L^{-1} $CoCl_2$, and 100 mmol·L^{-1} $CuCl_2$ + 400 mmol·L^{-1} $CoCl_2$ solutions, respectively.

2.2. Material characterizations

Powder X-ray diffraction (XRD) analysis was carried out on a Haoyuan DX-2800. X-ray diffractometer from 5° to 80° at a scanning rate of 5°/min. The surface morphology and structural characterizations were tested by scanning electron microscope (SEM, ZEISS Sigma 360) and transmission electron microscopy (TEM, JEM, 2100F). SEM and elemental mapping images tests were carried out on a Talos F200i instrument. The surface element compositions and detailed valence states of all samples were determined by X-ray photoelectron spectroscopy (XPS) on a Thermo Scientific K-Alpha instrument. The ultraviolet-visible (UV-vis) absorbance spectra were measured on a Puxi T700S instrument. The liquid product was measured by nuclear magnetic resonance spectroscopy (NMR, Bruker AV-600).

All X-ray absorption fine structure (XAFS) data were collected at BL11B beamline of Shanghai Synchrotron Radiation Facility (SSRF), located in China. The beam current of the storage ring was 200 mA in a top-up mode. The incident photons were monochromatized by a Si(111) double-crystal monochromator, with an energy resolution $\Delta E/E$ ~1.4×10^{-4}. The spot size at the sample was ~200 μm × 250 μm (H × V). The acquired X-ray absorption fine structure (EXAFS) data were normalized using the ATHENA module implemented in the Demeter software packages. The k^3-weighted $\chi(k)$ data were Fourier transformed to real (R) space using a hanning window (dk = 1.0 Å^{-1}) to separate the EXAFS contributions from different coordination shells. The ARTEMIS code was used to obtain the quantitative structural parameters by least-squares fitting.

2.3. Electrochemical measurements

Electrochemical measurements were carried on a Chenhua CHI-760E electrochemical workstation in an H-type electrolytic cell separated by a Nafion-117 proton exchange membrane. A piece of carbon paper (CP, 1 × 1 cm^2) coated with the as-prepared electrocatalyst (areal loading: 0.4 mg·cm^{-2}), a Pt disk electrode (1 × 1 cm^2) and a standard Ag/AgCl electrode were used as the working, counter and reference electrode, respectively. The proton exchange membrane was respectively treated in H_2O_2 (5 %) aqueous solution, deionized H_2O, and 0.5 mol·L^{-1} H_2SO_4 for 1 h at 80 °C before starting the electrochemical test. All potentials in this experiment were calibrated to reversible hydrogen electrode (RHE) by using the equation E (*vs.* RHE) = E (*vs.* Ag/AgCl) + 0.1989 + 0.059 × PH. In this study, all electrochemical measurements were carried out at room temperature.

2.4. Determination of ammonia

The concentration of ammonia in product solution was detected by the standard indophenol blue method. Typically, after chronoamperometry measurement, 2 mL of the product solution was collected from the cathode compartment of H-type cell, followed by the addition of 2 mL of 2 mol·L^{-1} NaOH solution containing 0.36 mol·L^{-1} salicylic acid and 0.19 mol·L^{-1} TCD was added. Then, 1 mL of 0.05 mol·L^{-1} NaClO and 0.2 mL of 1 wt% sodium nitroferricyanide (III) dihydrate solution was added into the above solution. The above solution was kept in the dark for 2 h, and then using UV-vis absorbance spectroscopy to measure the concentration of indophenol blue at a wavelength of 655 nm.

2.5. Determination of NO_2^-

5.0 mL of a 1 g·L^{-1} solution of *N*-(1-naphthyl) ethylenediamine dihydrochloride, along with 5.0 mL of glacial acetic acid, are introduced into a volumetric flask. Subsequently, the solution is made up to a total volume of 100 milliliters with a 5 g·L^{-1}

sulfanilamide solution to form a uniform solution and used as the chromogenic reagent. Then, 1.0 mL of electrolyte was collected from the cathode compartment and mixed with 4.0 mL of chromogenic reagent. After standing for 20 min in the dark for at room temperature, the light absorbance of the resulting solution was detected by an UV-Vis absorption spectrophotometer at a wavelength of 540 nm in the absorption spectrum.

2.6. Determination of hydrazine

Watt and Chrisp method were used to detect the possible N_2H_4 product in the electrolyte. Briefly, 30 mL of hydrochloric acid, 300 mL of ethanol and 5.99 g of para-(dimethylamino) benzaldehyde were mixed and regarded as a sensitive chromogenic reagent. Collecting 2 mL of electrolyte from the cathode compartment was mixed with 5 mL of the above chromogenic reagent. The lighting absorbance of the obtained solution was tested at a wavelength of 457 nm after standing for 20 min at room temperature.

2.7. ^{15}N isotope labelling experiments

To clarify the source of ammonia, the ^{15}N isotope labelling experiment was carried out using $Na^{15}NO_3$ ($Na^{15}NO_3$ with 98.3% enrichment, Sigma) as the feeding N source. 0.6 mL of the liquid product was collected from the cathode compartment and acidified with 0.1 mL of 0.1 mol·L^{-1} H_2SO_4 solution after the NITRR test for 1 h at −1.0 V *vs.* RHE in a 0.1 mol·L^{-1} Na_2SO_4 solution containing 500 ppm $^{15}NO_3^-$. Then, 550 μL of the above mixture was put into a NMR tube, and D_2O was added to a closed tube with a higher height of liquid level as a calibration sample for ^1H NMR analysis. The one-dimensional ^1H NMR spectra were collected by a superconducting Fourier transform NMR spectrometer (Bruker Avance-600).

2.8. Calculations of the NH_3 yield rates and Faradaic efficiencies (FE)

The NH_3 yield (Y_{NH3}) can be calculated as: Y_{NH3} (μg·h^{-1}·mg$^{-1}_{cat.}$) = (C_{NH3}×V)/(t×$m_{cat.}$), where C_{NH3} (μg·mL^{-1}) is the measured NH_3 concentration, V (mL) is the volume of the electrolyte, t (h) is the reaction time, and m (mg) is the catalyst loading mass on the CP. The FE can be calculated as: FE = (n×F×C_{NH3}×V)/(17×Q), where n is the number of transferred electrons, F is the Faraday constant (96485 C·mol^{-1}) and Q (C) is the total amount of applied electricity.

3. Results and discussion

3.1. Preparation and characterizations of samples

As shown in Fig. 1(a), various concentrations of cobalt-doped dendritic Cu with a surface enriched with Cu_2O/Cu heterojunctions (Co_x-Cu_2O/Cu, x = 0.05, 0.10, or 0.34) were synthesized *via* a rapid, convenient, energy-consumption-free, and green chemical replacement method. Specifically, at 25 °C in aqueous solution, the reduction electrode potential of Zn^{2+}/Zn (E^θ = −0.76 V *vs.* RHE) is notably lower than that of

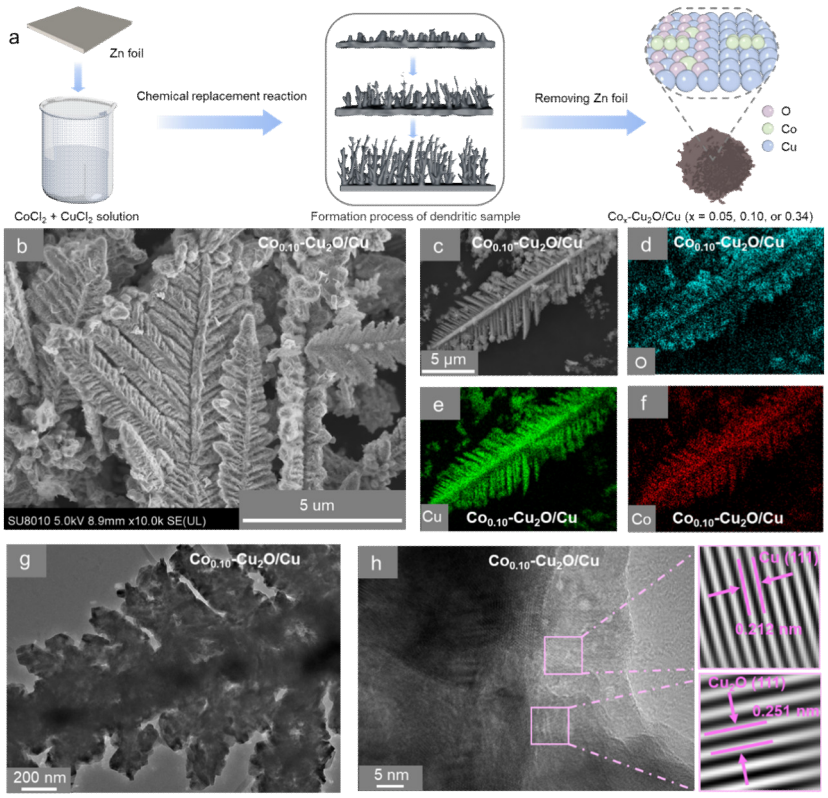

Fig. 1. Schematic diagram of the synthesis process, morphological and structural analysis of samples. (a) Schematic illustration of the preparation of Co_x-Cu_2O/Cu (x = 0, 0.05, 0.10, or 0.34) samples. SEM (b), element mapping images (c–f), TEM (g) and HR-TEM (h) images of Co_x-Cu_2O/Cu sample.

Cu^{2+}/Cu (E^{θ} = 0.34 V *vs.* RHE) and Co^{2+}/Co (E^{θ} = −0.28 V *vs.* RHE). Consequently, when a Zn foil is immersed in an aqueous solution containing $CuCl_2$ and $CoCl_2$, a spontaneous redox reaction occurs. Due to its higher reduction potential, Cu^{2+} is initially reduced by the Zn foil, which has a lower reduction potential, to form dendritic copper. Subsequently, portions of the Cu dendrites surface interact with oxygen components in the aqueous solution or air, leading to the formation of Cu_2O on the surface of dendritic Cu. This results in the creation of Cu_2O/Cu heterojunctions on the surface of dendritic Cu (Cu_2O/Cu). Following this, Co^{2+} is reduced and exists in the form of cobalt doping on the surface of the copper dendrites. As listed in Table S1, the molar ratio of $CuCl_2$ to $CoCl_2$ can be adjusted to synthesize dendrite Cu_2O/Cu with varying concentrations of cobalt doping (Co_x-Cu_2O/Cu, x = 0.05, 0.10, or 0.34). It is noteworthy that the production of Co_x-Cu_2O/Cu, with a yield exceeding 100 mg, can be achieved in just a few minutes using a Zn foil with an area of only 3 × 3 cm^2. If the contact area between the Zn foil and salt solution is increased, it is possible to achieve scalable mass production of the catalyst, with no adverse environmental impacts during the preparation process. Furthermore, compared to traditional electrodeposition methods or hydrothermal synthesis, the preparation of dendritic copper catalysts via the chemical displacement method does not require the consumption of electrical energy or other forms of energy. Therefore, compared to traditional electrodeposition methods or hydrothermal synthesis [50,51], the one-step chemical displacement method exhibits notable advantages, enabling the simple, rapid, energy-consumption-free, green and batch-scale synthesis of the Cu-based electrocatalyst with dendritic micro-nano-structures.

Initially, the surface morphological features of the samples were characterized using field-emission SEM. It is distinctly observable that the powder sample (Cu_2O/Cu) formed through the chemical displacement reaction between Zn foil and $CuCl_2$ solution exhibits a distinct pine-needle-like morphology, with lengths exceeding 5 micrometers (Figs. S1(a) and 1(b)). Specifically, the nanostructured dendrites comprise a prominent central spine encircled by a multitude of symmetrically arranged primary and secondary branches. Notably, not all primary branches achieve full development, resulting in a coexistence of both larger and smaller primary branches that are clearly observable. It is noteworthy that dendritic copper with cobalt doping also displays a prominent pine-needle-like morphology, indicating that cobalt doping has no significant impact in the surface morphology of the synthesized samples (Figs. 1(b) and 1(c)). The elemental mapping results presented in Figs. 1(d)–1(f) demonstrate a uniform distribution of Cu, O, and Co throughout the entire pine-needle-like dendritic copper structure. The aforementioned results indicate that Co has been uniformly doped into the dendritic copper structure through a one-step electrochemical displacement method. Fig. 1(g) displays TEM images of the $Co_{0.10}$-Cu_2O/Cu sample, revealing that the pine-needle-like morphology consists of numerous small fragments stacked together. This underscores that the dendritic samples possess a distinct and intricate three-dimensional (3D) structure, rather than being flat or two-dimensional. Such a complex 3D architecture is advantageous in the electrocatalytic NITRR process by enhancing the contact area between the electrolyte and catalyst, thereby effectively exposing the active sites. Upon closer examination of the $Co_{0.10}$-Cu_2O/Cu sample using high-resolution TEM (HRTEM, Fig. 1(h)), lattice spacings of 0.212 and 0.251 nm are observed, which correspond to the Cu (111) and Cu_2O (111) planes, respectively. This indicates that Cu and Cu_2O coexist on the surface of the dendritic Cu, forming a Cu_2O/Cu heterojunction structure. It is noteworthy that no lattice fringes associated with metallic cobalt or cobalt species were observed on the surface of the $Co_{0.10}$-Cu_2O/Cu sample in the HRTEM images. This could be attributed to cobalt species doped on the surface of dendritic copper existing in an atomic or amorphous phase. Moreover, as shown in Figs. S1(c) and S1(d), the TEM images of pristine Cu_2O/Cu also exhibit a similar 3D structure composed of numerous small fragments stacked together, and the presence of Cu_2O/Cu heterojunctions can be clearly observed.

To explore the crystalline structure of the resulting samples, XRD was implemented. The XRD patterns for the pristine Cu_2O/Cu, $Co_{0.05}$-Cu_2O/Cu, $Co_{0.10}$-Cu_2O/Cu, and $Co_{0.34}$-Cu_2O/Cu samples are depicted in Fig. 2(a). Dendritic Cu_2O/Cu displays prominent diffraction peaks at 43.2°, 50.3°, and 73.9°, which correspond to the (111), (200), and (220) planes of Cu, respectively. Additionally, diffraction peaks situated at 29.6°, 36.4°, 42.3°, 61.3°, and 73.5° are attributed to the (110), (111), (200), (220), and (311) planes of Cu_2O, respectively. With increasing Co doping concentration, the intensity of Cu_2O diffraction peaks progressively decreases. This manifestation is ascribed to redox reaction between the Co salt and Cu_2O on the dendritic copper surface, which consumes the surface Cu_2O and results in the formation of surface Co doping. In other words, Co species selectively interact with Cu_2O, facilitating the incorporation of Co at the Cu_2O/Cu heterojunction interface. Moreover, after doping Co species onto the surface of dendritic Cu, no additional peaks corresponding to metallic Co or other crystalline phases of Co species were observed in the XRD pattern of the sample. This absence of peaks likely suggests that the cobalt species doped on the surface exist in an atomic or amorphous phase, which aligns with the findings from HRTEM analysis. XPS was performed out to investigate elemental composition and valence states of as-obtained samples. As illustrated in Fig. 2(b), the high-resolution Cu 2*p* XPS spectrum of Cu_2O/Cu exhibits three characteristic peaks at 932.88, 934.20, and 935.59 eV corresponding to Cu^0, Cu^{+1} and Cu^{+2}, respectively. Meanwhile, a slight bending energy shift toward lower bending energy was observed as the dropped Co content decreasing, signifying that electron transfer of introducing Co species at Cu_2O/Cu interface. Besides, the Co 2*p* XPS peaks of $Co_{0.10}$-Cu_2O/Cu located at 780.94 and 782.96 eV assigned to Co^0 and Co^{2+} (Fig. 2(c)). It is notable that Co species binding energy increased with Co content gradual decrease, indicating forceful electron interaction between Cu and Co species that is propitious to absorb critical intermediate species improving the electrocatalytic activity.

X-ray absorption spectroscopy (XAS) was carried out to delve deeper into the intricate electronic structure and the

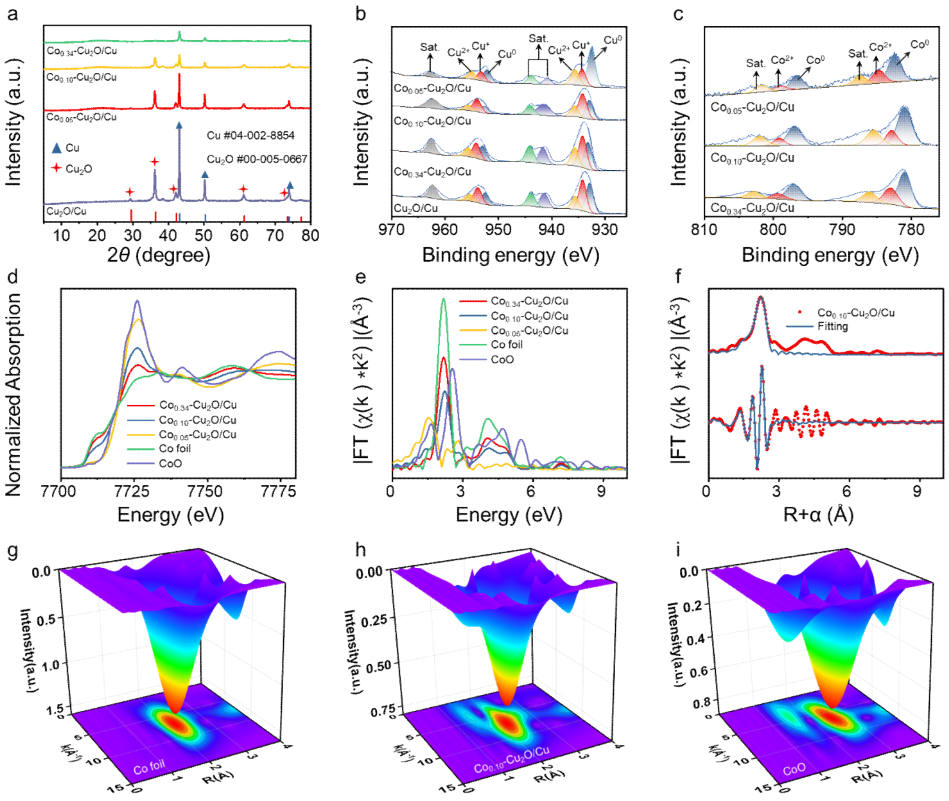

Fig. 2. Spectroscopic analysis of the samples. (a) XRD patterns of Co_x-Cu_2O/Cu (x = 0, 0.05, 0.10, or 0.34) samples. High-resolution XPS spectra at the Cu 2*p* (b) and Co 2*p* (c) edge. (d) Co *K*-edge XANES spectra. (e) Fourier transformations of the k_3-weighted χ(k)-function of the EXAFS spectra at Co K-edge. (f) Fitting results of the EXAFS spectra of $Co_{0.10}$-Cu_2O/Cu at K space and *R*-space, respectively. Wavelet transforms of the Cu K-edge and Co K-edge FT-EXAFS spectra of $Co_{0.10}$-Cu_2O/Cu (g), Co foil (h), and CoO (i).

coordination milieu surrounding the Co elements within Co_x-Cu_2O/Cu (x = 0.05, 0.10, 0.34) samples. According to XANES analysis results (Fig. 2(d)), $Co_{0.05}$-Cu_2O/Cu composite is situated in close proximity to CoO, exhibiting a more positive shift due to the presence of the Co–O bending signal. On the other hand, $Co_{0.10}$-Cu_2O/Cu is positioned between Co foil and CoO, suggesting a valence state for the Co species that lies between 0 and +2. Additionally, $Co_{0.34}$-Cu_2O/Cu overlaps with Co foil, indicating the presence of metallic Co. In addition, as shown in FT-EXAFS of Co species (Fig. 2(e)), $Co_{0.05}$-Cu_2O/Cu displays a coordination peak of Co–O bend at 1.52 Å in the first shell, which undergoes a negative shift compared with CoO standard sample, owning to Co substitutes abundant Cu in Cu_2O of Cu_2O/Cu forming the Co–O coordination structure. Meanwhile, $Co_{0.10}$-Cu_2O/Cu and $Co_{0.34}$-Cu_2O/Cu simultaneously show Co–Co signal at 2.18 and 2.22 Å, respectively, with a positive shift energy in contrast with Co foil (2.17 Å). This fact demonstrates that Co^{2+} was gradually reduce to form Co species as the increasing ratio of Co^{2+} element in the mixture of $CuCl_2$ and $CoCl_2$ solution. According to XANES and FT-EXAFS analysis results, the Co *K*-edge energy displays slightly shift, which may attribute to introducing Co in Cu_2O/Cu substrate leads to the change of electron structure. Thus, the electron transfer between Cu and Co was significantly strengthened, consistent with the XPS characterization analysis. To further explain detailed structure information of synthetic samples, the fitting results of the k^3-weighted FT EXAFS spectra were listed at Fig. 2(f), Fig. S2. and Table S2. This clearly suggests that Co different doped forms on the surface of Cu_2O/Cu with the different Co^{2+} concentrations. Firstly, the $Co_{0.05}$-Cu_2O/Cu sample obtained from the lowest content solution, massive Co replaced Cu atom in Cu_2O and a little of Co forms Cu-Co alloy. Subsequently, as the increasing of Co content, $Co_{0.10}$-Cu_2O/Cu exhibits visible Co–Co coordination environment but existing small Co species replaced Cu in Cu_2O. Besides, $Co_{0.34}$-Cu_2O/Cu only shows the Co–Co signal, revealing Co^{2+} reduced to pure substance. The detailed coordination environment information suggests Co^{2+} undergoes complex reduction under different $CoCl_2$ and $CuCl_2$ mixture solution, forming distinct forms of Co doped on Cu_2O/Cu (Co_x-Cu_2O/Cu). The aforementioned analytical results indicate that as the doping concentration of Co increases, its doping form transitions from an atomic state to a metallic state (Table S3). This implies that the doping form of Co within the dendritic copper structure can be modulated by altering its doping concentration. Moreover, the wavelet transforms analysis (WT) of Co *K*-edge FT EXAFS for $Co_{0.10}$-Cu_2O/Cu (Fig. 2(h)) reveal that the bonding mode Co is Co–Co (7.5 $Å^{-1}$) when in contrast with reference standard samples (Figs. 2(g) and 2(i)). Meanwhile, the WT of $Co_{0.05}$-Cu_2O/Cu and $Co_{0.34}$-Cu_2O/Cu (Fig. S3) corresponding to Co–O and Co–Co bend, respectively. The analysis result is exceedingly consistent with EXAFS analysis.

3.2. *Electrocatalytic NITRR Performances*

All electrochemical measurements were performed in a standardized H-type electrocatalytic cell (Fig. S4). The catalytic performance toward nitrate electroreduction was initially assessed by LSV. Fig. 3(a) reveals that $Co_{0.10}Cu_2O/Cu$ catalyst exhibits markedly elevated current density in a 0.1 mol·L^{-1} Na_2SO_4 solution with 500 ppm NO_3^- compared to a solution containing only 0.1 mol·L^{-1} Na_2SO_4 (from −0.5 to −0.9 V *vs.* RHE). The experimental observation points to the probable occurrence of the nitrate-to-ammonia conversion process in the Na_2SO_4 solution containing NO_3^-. In comparison to Cu_2O/Cu, $Co_{0.10}$-Cu_2O/Cu demonstrates a higher current density, potentially attributable to the Co sites facilitating the decomposition of H_2O. After conducting a 10-min chronoamperometry (CA) tests within the potential range from −0.5 to −0.9 V *vs.* RHE in the 0.1 mol·L^{-1} Na_2SO_4 solution containing 500 ppm NO_3^- (Fig. 3(b)), potential product ammonia in the cathodic electrolyte was quantitatively analyzed by the indophenol blue method (Fig. 3(c)). The NH_3 concentration in the product solution was quantitatively determined through the use of an ammonia standard curve (Fig. S5). The $Co_{0.10}$-Cu_2O/Cu sample demonstrated the highest yield rate of 290.0 μmol·h^{-1}mg$^{-1}_{cat.}$, along with a peak FE_{NH3} of 86.2% at −0.7 V *vs.* RHE for NH_3 synthesis (Figs. 3(d) and 3(e)). Moreover, as depicted in Fig. S6, the catalytic performances of the synthesized Cu_2O/Cu, $Co_{0.05}$-Cu_2O/Cu, and $Co_{0.34}$-Cu_2O/Cu catalysts were also systematically evaluated. At −0.8 V *vs.* RHE, the NH_3 yield and FE_{NH3} for $Co_{0.10}$-Cu_2O/Cu are significantly higher than those of Cu_2O/Cu (143.4 μmol·h^{-1}·mg$^{-1}_{cat.}$, and 61.2%, respectively), $Co_{0.05}$-Cu_2O/Cu (233.4 μmol·h^{-1}·mg$^{-1}_{cat.}$, and, 69.1% respectively), and $Co_{0.34}$-Cu_2O/Cu (243.0 μmol·h^{-1}·mg$^{-1}_{cat.}$ and 77.1%, respectively) (Figs. 3(d) and 3(e)). It is noteworthy that the doping of Co species into the Cu/Cu_2O heterojunction interfaces on the surface of dendritic copper significantly enhances both the NH_3 yield and FE_{NH3}. This could be attributed to the effective activation of H_2O molecules by cobalt species upon doping into the Cu/Cu_2O heterojunction interfaces, thereby furnishing abundant active hydrogen for NITRR. With an increase in the cobalt doping concentration, the cobalt species doped onto the surface of dendritic copper undergo a transition from atomic cobalt to metallic cobalt in its elemental form. However, the excessive formation of metallic cobalt in its elemental form on the surface of dendritic copper favors the HER reaction rather than enhancing NITRR. Consequently, as the cobalt doping concentration on the surface of dendritic copper increases, the NITRR performance exhibits a trend of initial enhancement followed by a subsequent decline. Moreover, as depicted in Fig.

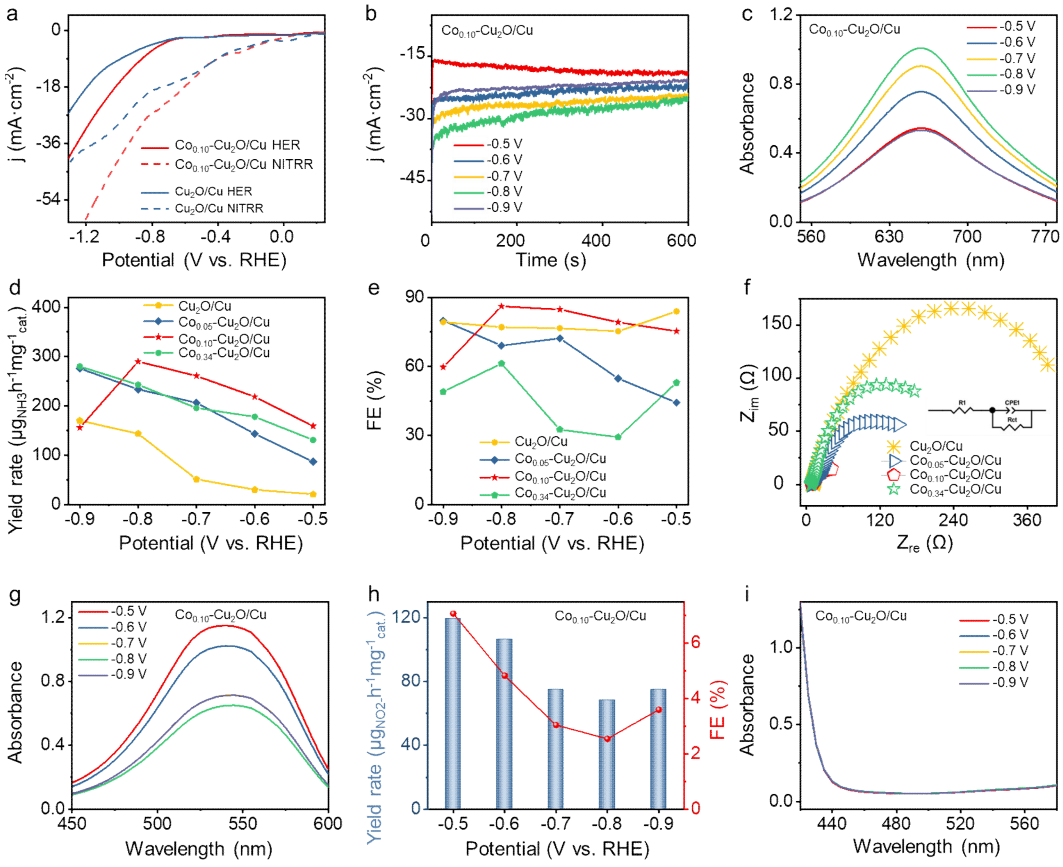

Fig. 3. Electrocatalytic NITRR performance of the synthesized samples. (a) LSV curves of $Co_{0.10}$-Cu_2O/Cu sample. (b) Time-dependent current density curves of $Co_{0.10}$-Cu_2O/Cu in 0.1 mol·L^{-1} Na_2SO_4 that contained 500 ppm NO_3^- for the NITRR. (c) UV-vis absorption spectra of the electrolyte after the NITRR test of $Co_{0.10}$-Cu_2O/Cu. The NH_3 yield (d) and corresponding FE_{NH3} values (e) of Cu_2O/Cu, $Co_{0.05}$-Cu_2O/Cu, $Co_{0.10}$-Cu_2O/Cu, and $Co_{0.34}$-Cu_2O/Cu samples. (f) Nyquist plots of Cu_2O/Cu, $Co_{0.05}$-Cu_2O/Cu, $Co_{0.10}$-Cu_2O/Cu, and $Co_{0.34}$-Cu_2O/Cu. (g) UV-vis absorption spectra of $Co_{0.10}$-Cu_2O/Cu after NITRR test for 10 min at various applied potentials and then coloured by the Griess indicator. (h) The NO_2^- yields and corresponding FE_{NO2-} values for $Co_{0.10}$-Cu_2O/Cu sample. (i) UV-vis absorption spectra of product solution after the NITRR test of $Co_{0.10}$-Cu_2O/Cu for 10 min at various applied potentials and then coloured by the para-dimethylamino-benzaldehyde indicator.

S7, within the tested range of NO_3^- concentrations (spanning from 100 to 1500 ppm), the NH_3 yield exhibits a significant increase, rising from 113.0 to 541.5 $\mu g \cdot h^{-1} \cdot mg^{-1}_{cat.}$. Meanwhile, the FE_{NH_3} consistently remains above 86% across all the NO_3^- concentrations examined. This demonstrates a strong correlation between the NH_3 yield and the nitrate concentrations, and highlights that the $Co_{0.10}$-Cu_2O/Cu catalyst maintains high selectivity over a broad range of NO_3^- concentrations, thereby presenting promising application potential in real wastewater. To further explore the underlying causes of the distinct NITRR performances exhibited by the samples, we conducted electrochemical impedance spectroscopy (EIS) measurements on Cu_2O/Cu, $Co_{0.05}$-Cu_2O/Cu, $Co_{0.10}$-Cu_2O/Cu, and $Co_{0.34}$-Cu_2O/Cu electrodes at −0.8 V *vs.* RHE (Fig. 3(f)).

The Nyquist plots obtained from all samples (Fig. 3(f)) were analyzed using the equivalent circuit model provided in the inset of Fig. 3(f) for determination of the charge transfer resistance (R_{ct}) values. Notably, equivalent series resistance (R_{ct}) values for $Co_{0.05}$-Cu_2O/Cu (40.38 Ω), $Co_{0.10}$-Cu_2O/Cu (13.27 Ω), and $Co_{0.34}$-Cu_2O/Cu (15.20 Ω) electrodes were significantly lower than that of the pristine Cu_2O/Cu electrode (54.14 Ω). This suggests that the Co_x-Cu_2O/Cu (x = 0.05, 0.10, or 0.34) electrodes exhibit lower R_{ct} and faster catalytic kinetics compared to the pristine Cu_2O/Cu electrode. The results of this analysis are consistent with the aforementioned NITRR test outcomes obtained from electrocatalysis. Moreover, according to our current knowledge, the NITRR performance of the $Co_{0.10}$-Cu_2O/Cu exhibits remarkable competitiveness in comparison with other electrocatalysts that have been reported in recent studies. (Table S4). Furthermore, potential byproducts such as NO_2^- in the electrolyte solution were identified using the Gress indicator method (Fig. S8). Figs. 3(g) and 3(h) illustrate that within the potential range of −0.5 to −0.9 V *vs.* RHE, the FE_{NO2-} decreases as the potential diminishes. This trend indicates that lower potentials favor further conversion of NO_2^-, thereby enhancing the performance of ammonia synthesis. Previous research has highlighted NO_3^--to-NO_2^- conversion has been recognized as the rate-limiting step in electrochemical NO_3^- reduction to NH_3, due to its slow kinetics. However, in this study, when the applied negative potential falls below −0.8 V *vs.* RHE, FE_{NO2-} remains below 3%. This finding suggests that the $Co_{0.10}$-Cu_2O/Cu catalyst effectively overcomes the energy barrier associated with rate-limiting step in the NITRR to NH_3, demonstrating high selectivity for this reaction. Furthermore, potential byproduct N_2H_4 was detected by the Watt and Chrisp method (Fig. S9), and Fig. 3(i) provides clear evidence that N_2H_4 was absent throughout the NITRR. These analytical results imply that $Co_{0.10}$-Cu_2O/Cu sample exhibits superior selectivity toward NH_3 production via NO_3^- electroreduction.

To ascertain the origin of the NH_3 product, a series of electrochemical tests were conducted. Firstly, a control experiment (Fig. 4(a)) was performed, involving the electrolysis of $Co_{0.10}$-Cu_2O/Cu in 0.1 $mol \cdot L^{-1}$ Na_2SO_4 solution at −0.8 V *vs.* RHE, no NH_3 production was observed in this experiment. An additional control electrolysis was performed using $Co_{0.10}$-Cu_2O/Cu in a 0.1 $mol \cdot L^{-1}$ Na_2SO_4 with 500 ppm NO_3^- solution at open-circuit potential (OCP), confirming the absence of ammonia production under these conditions. Besides, there is negligible ammonia production when bare carbon paper (CP) is employed as the cathode electrocatalyst. Furthermore, an ex-

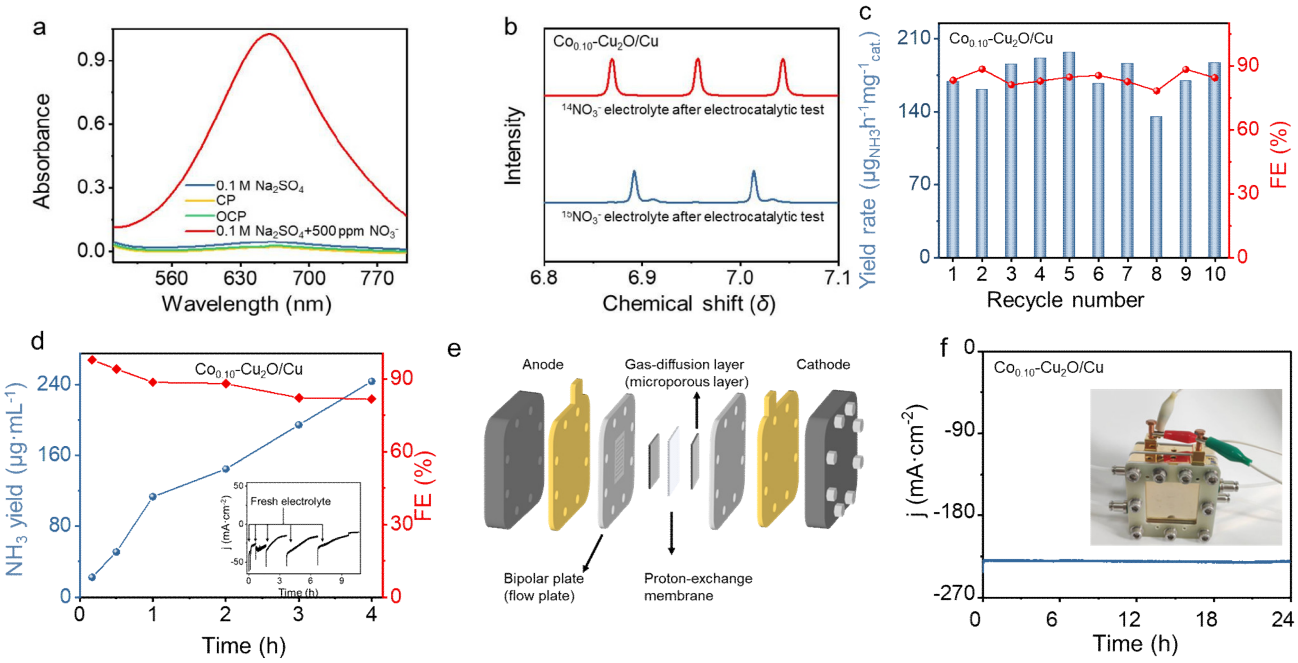

Fig. 4. (a) UV-vis absorption spectra of the product solution under various test conditions and then coloured by the indophenol indicator. (b) ^1H NMR spectra of product solution after NITRR test of $Co_{0.10}$-Cu_2O/Cu using $^{15}NO_3^-$ and $^{14}NO_3^-$ as the N-sources, respectively. (c) Cycling stability test of $Co_{0.10}$-Cu_2O/Cu at −0.8 V *vs.* RHE. (d) Time-dependent NH_3 concentration and corresponding FE_{NH3} after different reaction durations of $Co_{0.10}$-Cu_2O/Cu at a potential of −0.8 V *vs.* RHE. The inset in (d) shows the corresponding time-dependent current density curves of stability tests. (e) Schematic diagram of proton exchange membrane flow cell and flow field structure. (f) *I-t* curves of $Co_{0.10}$-Cu_2O/Cu conducted in a flow-type electrolytic cell, with the apparatus configuration depicted in the inset of Fig. 4(f).

periment utilizing ^{15}N-isotope labeling was conducted by employing $^{15}NO_3^-$ as the nitrogen source. Fig. 4(b) displays the ^1H NMR spectrum of the electrolyte, revealing characteristic double peaks corresponding to $^{15}NH_4^+$ derived from the labeled $Na^{15}NO_3$. Additionally, the presence of a triplet coupling peak for $^{14}NH_4^+$ in the spectrum, when $^{14}NO_3^-$ was used as the initial nitrogen source, further validated that the ammonia synthesized was a product of the NO_3^- electroreduction. Stability serves as a fundamental metric for assessing in electrocatalytic performance. Hence, an investigation into the durability of the $Co_{0.10}$-Cu_2O/Cu sample for NITRR was conducted, with the experiments carried out in a solution containing 0.1 mol·L^{-1} Na_2SO_4 with NO_3^-. Fig. 4(c) illustrate that after 10 consecutive cyclic tests, neither the ammonia production rate nor the FE_{NH3} of the $Co_{0.10}$-Cu_2O/Cu sample showed a significant change, suggesting its sustained NITRR performance. Moreover, the long-term stability of $Co_{0.10}$-Cu_2O/Cu was evaluated. Fig. 4(d) demonstrates that as the electrolysis duration increased, the ammonia concentration rose correspondingly. Following a two-hour NITRR durability assessment, a decline in FE_{NH3} was observed, attributable to the diminished NO_3^- concentration within the electrolyte solution. Moreover, the inset in Fig. 4(d) highlights that the current density remains largely stable throughout the extensive durability testing of the $Co_{0.10}$-Cu_2O/Cu catalyst. These analytical results imply that continuous NH_3 production is achievable via the consumption of dissolved NO_3^- in the electrolyte, thereby verifying the outstanding durability of $Co_{0.10}$-Cu_2O/Cu during NITRR. To assess the commercial viability of $Co_{0.10}$-Cu_2O/Cu for continuous electrocatalytic reactor systems, we tested its NITRR activity in a flow-type electrolytic cell system (Fig. 4(e) and inset in Fig. 4(f)). As depicted in Fig. 4(f), the catalyst maintained a high current density exceeding 240 mA·cm^{-2} at −0.8 V *vs.* RHE and exhibited remarkable stability over a 24-h period.

3.3. Exploration of the origin of the high-performance electrocatalyst

In-situ infrared spectra analysis was employed to monitor the key activity intermediates on the surface of the $Co_{0.10}$-Cu_2O/Cu sample during electrochemical NITRR. Fig. 5(a) shows characteristic peaks of $*NO_3H$ and *NO at 1702 and 1643 cm^{-1}, indicating the continuous deoxygenation process of NITRR. Subsequently, a distinct characteristic peak observed at

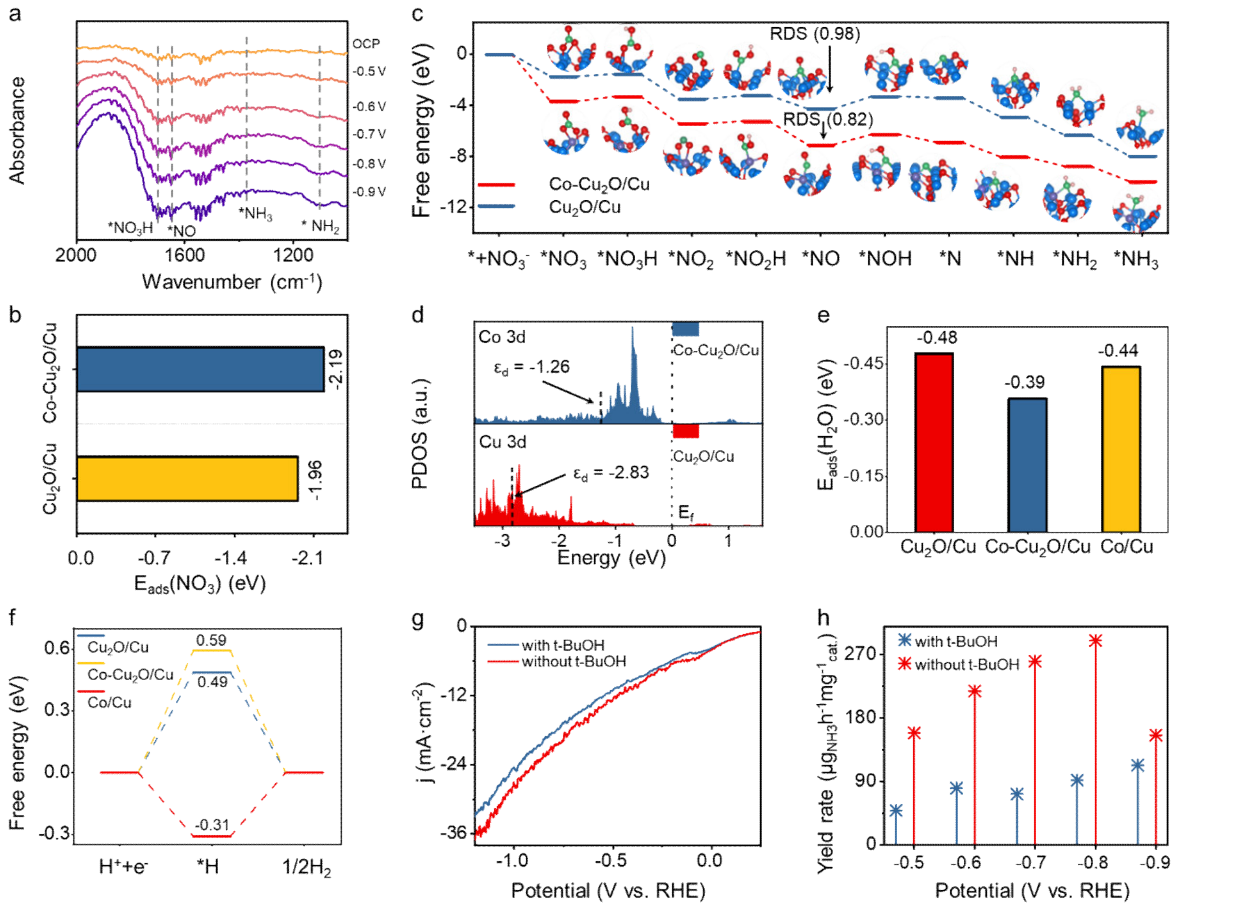

Fig. 5. (a) *In-situ* infrared spectra of $Co_{0.10}$-Cu_2O/Cu sample at different negative applied potentials in the 0.1 mol·L^{-1} Na_2SO_4 electrolytes containing 500 ppm NO_3^-. (b) Adsorption energies of NO_3^- on Cu_2O/Cu and cobalt-doped Cu_2O/Cu (Co-Cu_2O/Cu). (c) Free energy diagrams of possible NITRR pathways on Cu_2O/Cu and Co-Cu_2O/Cu surfaces, respectively. (d) PDOS of Co 3*d* in Co-Cu_2O/Cu and that of Cu 3*d* in Cu_2O/Cu. (e) Comparison of adsorption energy of H_2O on the surfaces of Cu_2O/Cu, Co-Cu_2O/Cu and Co/Cu, respectively. (f) Free energy diagram for HER on Cu_2O/Cu, Co-Cu_2O/Cu and Co/Cu surfaces. (g) LSV curves of $Co_{0.10}$-Cu_2O/Cu in 0.1 mol·L^{-1} Na_2SO_4 and 500 ppm NO_3^- with or without 0.5 mol·L^{-1} TBA. (h) NH_3 yield of $Co_{0.10}$-Cu_2O/Cu at given potentials for the NITRR with or without 0.5 mol·L^{-1} TBA.

approximately 1100 cm^{-1} is attributed to $*NH_2$ stretching vibrations, indicating the occurrence of a hydrogenation-dehydrogenation process. According to above analysis, deoxygenation and hydrogenation is indispensable for NITRR, so the *H species play a vital role for ammonia synthesis. Meanwhile, as the applied potential increasing, the intensity of $*NH_3$ absorption peak (1336 cm^{-1}) gradually strengthened, implying NO_3^- successfully transform to NH_3. Generally, *in-situ* infrared spectroscopy is limited to capturing the signals of certain crucial reactive intermediates. Therefore, a systematic investigation of the detailed reaction pathways necessitates the use of theoretical calculations. The density functional theory (DFT) calculations were implemented to further probe possible active sites and NITRR pathways. Based on the analysis results of structural characterization for Co_x-Cu_2O/Cu (x = 0.05, 0.10, or 0.34), the optimized models of the Cu_2O/Cu heterojunction (Fig. S10) and Co-doped Cu_2O/Cu heterojunction (Co-Cu_2O/Cu) (Fig. S11), were established. Since the adsorption behavior of NO_3^- on the catalysts is of crucial significance for the selective catalysis of NITRR, we initially investigated the adsorption energy of NO_3^- on the Cu_2O/Cu and Co–Cu_2O/Cu surfaces. Fig. 5(b) illustrates that the computed adsorption energy (E_{ads}) of NO_3^- in Cu_2O/Cu and Co-Cu_2O/Cu is −1.96 and −2.19 eV, respectively. A negative E_{ads} value implies that the adsorption process is exothermic. Furthermore, the occurrence of adsorption becomes more facilitated as the adsorption energy decreases. Notably, it is observable that NO_3^- exhibits a greater propensity for adsorption on the Co-Cu_2O/Cu surface, aligning consistently with the experimental findings. In other words, the incorporation of Co into the Cu_2O/Cu heterojunction interface enhances the adsorption process of NO_3^-. Fig. 5(c) displays the Gibbs free energy profiles during the NITRR on the surface of Co-Cu_2O/Cu, accompanied by the profiles for Cu_2O/Cu for purposes of comparison. The transition from *NO to *NOH represents the rate-determining step (RDS) for both Cu_2O/Cu and Co-Cu_2O/Cu during the NITRR. Notably, the ΔG value associated with this RDS is positive and highest throughout the entire NITRR process. It is evident that the reaction free energy for the *NO hydrogenation step is lower on Co-Cu_2O/Cu (0.82 eV) compared to Cu_2O/Cu (0.98 eV). This suggests that the incorporation of cobalt sites into Cu_2O/Cu reduces the reaction energy barrier of the RDS, thereby facilitating the ammonia production process during NITRR.

Moreover, as shown in Fig. 5(d), the projected density of states (PDOS) and *d*-band centers of Cu_2O/Cu and Co-Cu_2O/Cu catalysts were also calculated. The *d* band center (ε_d) of the Co site in Co-Cu_2O/Cu is −1.25 eV, being closer to the Fermi level than that of the Cu site in Cu_2O/Cu. The higher d-band center of the Co site enhances the binding of NO_3^- on Co-Cu_2O/Cu surface, thus facilitating the adsorption of NO_3^-. During the NITRR process, the active sites and electrons on the surface might be occupied and consumed by H_2O molecules, leading to a decline in the catalytic efficiency of NITRR. Hence, the adsorption energy of H_2O molecule on the different catalyst surface was calculated. As depicted in Fig. 5(e), the adsorption energy of H_2O on the Co-Cu_2O/Cu is higher than that of pure Cu_2O/Cu, suggesting that Co doping is beneficial for inhibiting the adsorption of water molecules. However, as the doping concentration of Co increases, the adsorption of water molecules intensifies upon the emergence of pure cobalt on the surface, potentially constituting a contributing factor to the decline in electrocatalytic performance. Moreover, Fig. 5(f) demonstrates that the doping concentration of Co exerts a notable influence on HER activity. Specifically, a moderate cobalt doping concentration facilitates the water dissociation, which in turn leads to formation of active hydrogen. Conversely, at higher Co doping concentrations, where a greater amount of metallic cobalt forms on the dendritic Cu surface, the HER activity is significantly enhanced. This, in turn, decreases the utilization rate of *H during the NITRR process, ultimately resulting in reduced selectivity for ammonia synthesis *via* NITRR. Analysis of the aforementioned computational results indicates that modulating the Co doping concentration can markedly adjust the concentration of active hydrogen at the Cu_2O/Cu heterojunction interface, thereby exerting an influence on the dynamic equilibrium between *H generation and consumption in the NITRR process. To verify the importance of active hydrogen for ammonia production during NITRR, we captured the active hydrogen on the catalyst surface using tertiary butyl alcohol (TBA) and observed its impact on the performance of NITRR. Obviously, as showed in Fig. 5(g), with the addition of TBA, LSV current density of Co-Cu_2O/Cu obviously decreased and the corresponding NH_3 yield similarly reduced (Fig. 5(h)). The aforementioned experimental phenomena demonstrate that active hydrogen is crucial for NH_3 synthesis in the NITRR process, and its concentration significantly affects the FE_{NH3}. Excessively high concentrations can trigger vigorous HER side reactions, leading to a reduction in FE_{NH3}. Conversely, insufficient concentrations impede the smooth progression of NH_3 synthesis in the electrochemical NITRR process. Therefore, the key to elevating the selectivity of NH_3 synthesis in the electrochemical NITRR process is controlling the concentration of active hydrogen on the catalyst surface, which in turn maintains a dynamic equilibrium between its generation and consumption.

4. Conclusions

In summary, we report the preparation of nano-dendritic heterojunction structures (Co_x-Cu_2O/Cu, x = 0.05, 0.10, or 0.34) doped with different concentrations of cobalt, employing a convenient, energy-consumption-free, and environmentally friendly chemical replacement method. By varying the doping concentration of Co, we have achieved a controllable transition of Co doping at the Cu_2O/Cu heterojunction interfaces, from an atomic state to metallic cobalt. The integration of experimental results and theoretical calculations suggests that doping cobalt in its atomic form enhances adsorption of nitrate reaction species onto the catalyst surface, whereas doping with metallic cobalt promotes generation of active hydrogen. By modulating cobalt doping concentrations at the Cu_2O/Cu heterojunction interfaces of dendritic copper surfaces, we achieve precise control over the dynamic equilibrium between active hydrogen production and its consumption, thereby optimizing NITRR performance. Our work provides valuable insights and serves

as a reference for the subsequent design of high-performance copper-based catalysts, particularly in the area of enhancing NITRR selectivity through the modulation of active hydrogen concentrations on the copper-based catalyst surface via adjusting the metal doping form.

Electronic supporting information

Supporting information is available in the online version of this article.

References

[1] M. Jiang, X. Chen, F. Chen, M. Wang, X. Luo, Y. He, C. Wu, L. Zhang, X. Li, X. Liao, Z. Jiang, Z. Jin, *Chem*, **2025**, 11, 102441.

[2] J. W. Erisman, M. A. Sutton, J. Galloway, Z. Klimont, W. Winiwarter, *Nat. Geosci.*, **2008**, 1, 636–639.

[3] H. Xu, Y. Ma, J. Chen, W.-X. Zhang, J. Yang, *Chem. Soc. Rev.*, **2022**, 51, 2710–2758.

[4] M. Jiang, X. Huang, D. Luo, C. Tian, Z. Jin, *Nano Energy*, **2025**, 135, 110683.

[5] G.-F. Chen, Y. Yuan, H. Jiang, S.-Y. Ren, L.-X. Ding, L. Ma, T. Wu, J. Lu, H. Wang, *Nat. Energy*, **2020**, 5, 605–613.

[6] F.-Y. Chen, Z.-Y. Wu, S. Gupta, D. J. Rivera, S. V. Lambeets, S. Pecaut, J. Y. T. Kim, P. Zhu, Y. Z. Finfrock, D. M. Meira, G. King, G. Gao, W. Xu, D. A. Cullen, H. Zhou, Y. Han, D. E. Perea, C. L. Muhich, H. Wang, *Nat. Nanotechnol.*, **2022**, 17, 759–767.

[7] M. Jiang, L. Han, P. Peng, Y. Hu, Y. Xiong, C. Mi, Z. Tie, Z. Xiang, Z. Jin, *Nano Lett.*, **2022**, 22, 372–379.

[8] D. Hao, Z.-G. Chen, M. Figiela, I. Stepniak, W. Wei, B.-J. Ni, *J. Mater. Sci. Technol.*, **2021**, 77, 163–168.

[9] M. Jiang, A. Tao, Y. Hu, L. Wang, K. Zhang, X. Song, W. Yan, Z. Tie, Z. Jin, *ACS Appl. Mater. Interfaces*, **2022**, 14, 17470–17478.

[10] S. Ye, Z. Chen, G. Zhang, W. Chen, C. Peng, X. Yang, L. Zheng, Y. Li, X. Ren, H. Cao, D. Xue, J. Qiu, Q. Zhang, J. Liu, *Energy Environ. Sci.*, **2022**, 15, 760–770.

[11] M. Jiang, M. Zhu, J. Ding, H. Wang, Q. Yu, X. Chen, Y. He, M. Wang, X. Luo, C. Wu, L. Zhang, X. Yao, H. Wang, X. Li, X. Liao, Z. Jiang, Z. Jin, *J. Hazard. Mater.*, **2024**, 476, 134909.

[12] J. Liang, Z. Li, L. Zhang, X. He, Y. Luo, D. Zheng, Y. Wang, T. Li, H. Yan, B. Ying, S. Sun, Q. Liu, M. S. Hamdy, B. Tang, X. Sun, *Chem*, **2023**, 9, 1768–1827.

[13] W. J. Rogan, M. T. Brady, *Pediatrics*, **2009**, 123, e1123–e1137.

[14] F. Chen, X. Zhou, H. Wang, X. Liu, Q. Yang, X. Chen, Q. Mu, J. Liu, X. Li, X. Liao, Z. Jiang, Z. Jin, M. Jiang, *Adv. Funct. Mater.*, **2025**, 35, 2421405.

[15] M. Jiang, J. Su, X. Song, P. Zhang, M. Zhu, L. Qin, Z. Tie, J.-L. Zuo, Z. Jin, *Nano Lett.*, **2022**, 22, 2529–2537.

[16] S.-J. Qian, H. Cao, X.-M. Lv, J. Li, Y.-G. Wang, *J. Am. Chem. Soc.*, **2025**, 147, 21032–21040.

[17] W. Zhu, F. Yao, Q. Wu, Q. Jiang, J. Wang, Z. Wang, H. Liang, *Energy Environ. Sci.*, **2023**, 16, 2483–2493.

[18] X. Chen, F. Chen, X.-Y. Zhong, J. Ding, H. Wang, L. Dai, X. Ma, H. Wang, C. Wu, X. Li, Y. Xiong, Z. Jin, M. Jiang, *J. Energy Chem.*, **2025**, 110, 768–777.

[19] S. Han, H. Li, T. Li, F. Chen, R. Yang, Y. Yu, B. Zhang, *Nat. Catal.*, **2023**, 6, 402–414.

[20] J. Wang, J. Cai, K.-X. Ren, L. Liu, S.-J. Zheng, Z.-Y. Wang, S.-Q. Zang, *Sci. Adv.*, **2024**, 10, eadn7556.

[21] Z. Shen, G. Chen, X. Cheng, F. Xu, H. Huang, X. Wang, L. Yang, Q. Wu, Z. Hu, *Sci. Adv.*, **2024**, 10, eadm9325.

[22] M. Jiang, Q. Zhu, X. Song, Y. Gu, P. Zhang, C. Li, J. Cui, J. Ma, Z. Tie, Z. Jin, *Environ. Sci. Technol.*, **2022**, 56, 10299–10307.

[23] Y. Li, Y. Bai, Y. Wang, S. Lu, L. Fang, *Environ. Res.*, **2025**, 266, 120422.

Graphical Abstract

Chin. J. Catal., 2025, 79: 78–90 doi: 10.1016/S1872-2067(25)64848-0

Optimized kinetic pathways of active hydrogen generation at Cu_2O/Cu heterojunction interfaces to enhance nitrate electroreduction to ammonia

Xi Chen, Wei Jin, Xinyu Zhong, Hongqiao Lin, Junjie Ding, Xinyu Liu, Hui Wang, Fasheng Chen, Yan Xiong *, Changchun Ding *, Zhong Jin *, Minghang Jing *

Xihua University; Nanjing University; Shanghai Institute of Applied Physics, Chinese Academy of Sciences; Chongqing University

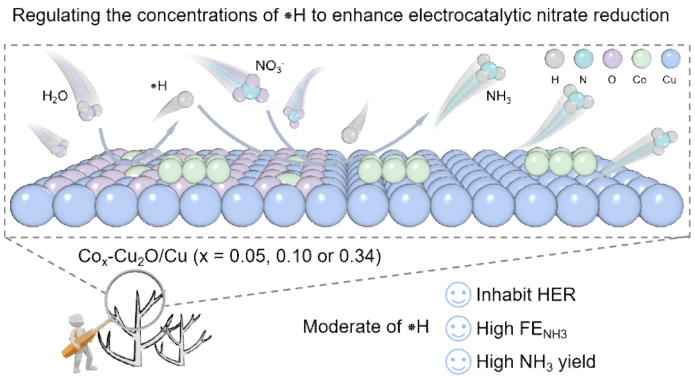

The synthesis of nano-dendritic Cu_2O/Cu heterojunction doped with varying concentrations of cobalt via a chemical replacement method. This approach optimizes the kinetic pathways for *H generation, thereby enhancing the selectivity of nitrate electroreduction to ammonia.

[24] S. Lu, *Precis. Chem.*, **2025**, https://doi.org/10.1021/prechem.5c00038.
[25] P. Li, R. Li, Y. Liu, M. Xie, Z. Jin, G. Yu, *J. Am. Chem. Soc.*, **2023**, 145, 6471–6479.
[26] P. Li, L. Liao, Z. Fang, G. Su, Z. Jin, G. Yu, *Proc. Natl. Acad. Sci. U. S. A.*, **2023**, 120, e2305489120.
[27] Q. Yan, R. Zhao, L. Yu, Z. Zhao, L. Liu, J. Xi, *Adv. Mater.*, **2024**, 36, 2408680.
[28] Y. Li, Q. Zhang, H. Dai, D. He, Z. Ke, X. Xiao, *Energy Environ. Sci.*, **2024**, 17, 9233–9243.
[29] Z. Shen, Y. Yu, Z. Zhao, S. Zhang, S. Xu, S. Yang, Y. Hu, *J. Hazard. Mater.*, **2023**, 445, 130651.
[30] L. Fang, S. Wang, C. Song, S. Lu, X. Yang, X. Qi, H. Liu, *Chem. Eng. J.*, **2022**, 446, 137341.
[31] X. Fu, X. Zhao, X. Hu, K. He, Y. Yu, T. Li, Q. Tu, X. Qian, Q. Yue, M. R. Wasielewski, Y. Kang, *Appl. Mater. Today*, **2020**, 19, 100620.
[32] Y. Fu, S. Wang, Y. Wang, P. Wei, J. Shao, T. Liu, G. Wang, X. Bao, *Angew. Chem. Int. Ed.*, **2023**, 62, e202303327.
[33] R. Daiyan, T. Tran-Phu, P. Kumar, K. Iputera, Z. Tong, J. Leverett, M. H. A. Khan, A. Asghar Esmailpour, A. Jalili, M. Lim, A. Tricoli, R.-S. Liu, X. Lu, E. Lovell, R. Amal, *Energy Environ. Sci.*, **2021**, 14, 3588–3598.
[34] Z. Gu, Y. Zhang, X. Wei, Z. Duan, Q. Gong, K. Luo, *Adv. Mater.*, **2023**, 35, 2303107.
[35] J. Yu, R.-T. Gao, X. Guo, N. Truong Nguyen, L. Wu, L. Wang, *Angew. Chem. Int. Ed.*, **2025**, 64, e202415975.
[36] Y. Wang, A. Xu, Z. Wang, L. Huang, J. Li, F. Li, J. Wicks, M. Luo, D.-H. Nam, C.-S. Tan, Y. Ding, J. Wu, Y. Lum, C.-T. Dinh, D. Sinton, G. Zheng, E. H. Sargent, *J. Am. Chem. Soc.*, **2020**, 142, 5702–5708.
[37] X. Yang, R. Wang, S. Wang, C. Song, S. Lu, L. Fang, F. Yin, H. Liu, *Appl. Catal. B*, **2023**, 325, 122360.
[38] S. Zhang, J. Wu, M. Zheng, X. Jin, Z. Shen, Z. Li, Y. Wang, Q. Wang, X. Wang, H. Wei, J. Zhang, P. Wang, S. Zhang, L. Yu, L. Dong, Q. Zhu, H. Zhang, J. Lu, *Nat. Commun.*, **2023**, 14, 3634.
[39] L. Wu, J. Feng, L. Zhang, S. Jia, X. Song, Q. Zhu, X. Kang, X. Xing, X. Sun, B. Han, *Angew. Chem. Int. Ed.*, **2023**, 62, e202307952.
[40] Y. Liu, Z. Zhuang, Y. Liu, N. Liu, Y. Li, Y. Cheng, J. Yu, R. Yu, D. Wang, H. Li, *Angew. Chem. Int. Ed.*, **2024**, 63, e202411396.
[41] J. Wang, Z. Ou, C. Dong, M. Su, A. Ali, A. V. Kuklin, H. Ågren, G. V. Baryshnikov, Y. Liu, X. Zhao, H. Zhang, *ACS Catal.*, **2025**, 15, 156–166.
[42] M. Luo, Z. Wang, Y. C. Li, J. Li, F. Li, Y. Lum, D.-H. Nam, B. Chen, J. Wicks, A. Xu, T. Zhuang, W. R. Leow, X. Wang, C.-T. Dinh, Y. Wang, Y. Wang, D. Sinton, E. H. Sargent, *Nat. Commun.*, **2019**, 10, 5814.
[43] X.-Y. Ji, K. Sun, Z.-K. Liu, X. Liu, W. Dong, X. Zuo, R. Shao, J. Tao, *Nano-Micro Lett.*, **2023**, 15, 110.
[44] H. Jiang, G.-F. Chen, O. Savateev, J. Xue, L.-X. Ding, Z. Liang, M. Antonietti, H. Wang, *Angew. Chem. Int. Ed.*, **2023**, 62, e202218717.
[45] Y. Wang, Y. Xu, C. Cheng, B. Zhang, B. Zhang, Y. Yu, *Angew. Chem. Int. Ed.*, **2024**, 63, e202315109.
[46] H. Li, S. Li, R. Guan, Z. Jin, D. Xiao, Y. Guo, P. Li, *ACS Catal.*, **2024**, 14, 12042–12050.
[47] W. Yang, Z. Chang, X. Yu, P. Wu, R. Shen, L. Wang, X. Cui, J. Shi, *Adv. Sci.*, **2025**, 12, 2416386.
[48] Y. Zhou, R. Duan, H. Li, M. Zhao, C. Ding, C. Li, *ACS Catal.*, **2023**, 13, 10846–10854.
[49] F. Chen, X.-Y. Zhong, J. Ding, X. Chen, X. Liao, Z. Jiang, Y. Xiong, Z. Jin, M. Jiang, *J. Colloid Interface Sci.*, **2026**, 701, 138664.
[50] H. Ma, J. Yan, J. Xu, P. Chen, J. Qi, Y. Ding, S. Zhang, L. Lu, *J. Hazard. Mater.*, **2024**, 470, 134261.
[51] Y.-Z. Xu, D. F. Abbott, R. N. Dürr, T. N. Huan, V. Mougel, *Adv. Energy Mater.*, **2024**, 2402294.

优化Cu_2O/Cu异质结界面处活性氢产生的动力学路径用于增强硝酸盐电还原产氨

陈　羲[a,1], 金　伟[a,1], 钟信宇[c], 林虹巧[b], 丁俊杰[d], 刘欣予[a], 王　慧[a], 陈法升[a], 熊　衍[b,*], 丁长春[a,*], 金　钟[b,*], 江明航[a,b,*]

[a]西华大学理学院化学系, 四川成都610039

[b]南京大学化学化工学院, 绿色化学与工程研究院, 天长新材料与能源技术研发中心, 苏州市新能源材料与器件绿色智能制造重点实验室, 江苏省清洁能源催化与智能绿色化工重点实验室, 介观化学教育部重点实验室, 高性能高分子材料与技术教育部重点实验室, 配位化学国家重点实验室, 江苏南京210023

[c]中国科学院上海应用物理研究所, 上海201800

[d]重庆大学物理学院量子材料与器件中心, 重庆401331

摘要: 氨(NH_3)是氮肥、医药及其他重要工业产品生产过程中的关键基础化学品. 本文旨在通过电催化硝酸盐还原反应(NITRR), 将环境中的硝酸盐污染物转换为具有工业附加值的NH_3, 既解决了硝酸盐污染的问题, 又实现了氮资源的循环利用. 然而, 电化学NITRR涉及复杂的多电子转移反应步骤和缓慢的动力学过程. 同时, 竞争性析氢反应(HER)和含氮副产物的产生, 导致额外的电能消耗, 降低了NITRR产NH_3的选择性和能量效率. 因此, 设计和制备具有高选择性NITRR电催化剂, 仍然是电催化领域的热点研究课题. 目前, 铜(Cu)基催化剂由于其独特的外层电子构型($3d^{10}$), 是实现高选择性电催化NITRR为NH_3最具潜力的电极材料. 然而, Cu基材料对水分子活化产活性氢(*H)的能力较弱, 从而阻碍了电化学NITRR过程中所必需*H产生的动力学过程. 鉴于钴(Co)基催化剂有利于水分子活化产生*H, 故利用Co掺杂Cu基催化剂调节电化学NITRR过程中*H浓度, 以提升NH_3的产率和选择性是本文的主要研究思路.

本文通过一种简单、快速、环境友好且无能耗的化学置换法, 制备了一系列具有不同Co掺杂浓度的纳米枝晶状Cu_2O/Cu异质结材料(Co_x-Cu_2O/Cu, x = 0.05, 0.10或0.34). 通过调控Co的掺杂浓度, 成功实现了Cu_2O/Cu异质结界面处Co掺杂形式从原子态向单质态的可控转变. 实验结合理论计算研究表明, 掺杂原子态Co增强了硝酸根在催化剂表面的吸附强度, 而掺杂单质态Co有利于*H的生成. *H是NITRR合成NH_3的关键活性物种, 其浓度对法拉第效率(FE_{NH3})有显著影响. 具体来说, *H的浓度不足会减缓NITRR产NH_3的动力学过程, 而浓度过高则会诱发剧烈的HER副反应, 导致产NH_3选择性降低. 因此, 调控Cu基催化剂表面的*H浓度, 使其在NITRR产NH_3过程中达到产生和消耗之间的动态平衡是至关重要的. 因

此, 通过对纳米枝晶状Cu_2O/Cu异质结材料中掺杂Co浓度的调节, 实现了Co掺杂形式(原子态和单质态)比例的调控, 从而能有效地调节枝晶状Cu_2O/Cu异质结材料界面处*H的浓度. 得益于Cu_2O/Cu异质结界面处*H浓度的调节, 使得电化学NITRR产NH_3过程中*H的产生和消耗之间维持了动态平衡, 从而显著促进了电化学NITRR产NH_3的动力学过程. 基于上述优势, 所制$Co_{0.10}$-Cu_2O/Cu催化剂在−0.7 V *vs.* RHE的电压下, 电化学NITRR为NH_3的产率为290.0 μmol·h^{-1}·mg$^{-1}_{cat}$, FE_{NH3}为86.2%, 其性能显著高于初始的Cu_2O/Cu催化剂的性能(NH_3的产率为51.0 μmol·h^{-1}·mg$^{-1}_{cat}$, FE_{NH3} = 32.5%). 此外, $Co_{0.10}$-Cu_2O/Cu催化剂表现出显著的稳定性, 在连续的循环稳定性测试和长时间耐久性评估中, 其催化活性无明显衰减.

综上, 本工作通过一种简单快速的化学置换法在Cu_2O/Cu异质结界面处掺杂不同浓度的Co, 有效调节了催化剂表面的*H浓度, 进而提升了电催化硝酸盐还原产NH_3的选择性, 为后续设计和合成高效Cu基催化剂以及优化催化剂表面*H产生的动力学路径以提升NITRR性能, 提供了一定的实验和理论参考.

关键词: 活性氢浓度调节; 调控Co的掺杂形式; 电催化硝酸根还原; 电催化合成氨

收稿日期: 2025-07-04. 接受日期: 2025-08-23. 上网时间: 2025-12-05.

*通讯联系人. 电子信箱: xiongyan@nju.edu.cn (熊衍), ccding626@163.com (丁长春), zhongjin@nju.edu.cn (金钟), minghang@mail.xhu.edu.cn (江明航).

[1]共同第一作者.

基金来源: 国家自然科学基金(22561160129, 22479074, 22475096); 四川省自然科学基金(2023NSFSC1074, 2023NSFSC0909); 西华大学人才引进项目(Z222051); 装备预研与教育部联合基金一般项目(8091B02052407); 江苏省基础研究计划重点项目(BK20253008); 江苏省自然科学基金(BK20240400, BK20241236); 江苏省科技重大专项(BG2024013); 江苏省科技成果转化专项基金(BA2023037); 江苏省学位与研究生教育改革项目(JGKT24_C001); 苏州市关键核心技术公开竞赛项目(SYG2024122); 苏州实验室开放研究基金(SZLAB-1308-2024-TS005); 郴州国家可持续发展议程创新示范区重大科技攻关项目(2023sfq11).